

Defective TiO_{2-x} for High-Performance Electrocatalytic NO Reduction toward Ambient NH_3 Production

Zixiao Li, Qiang Zhou, Jie Liang, Longcheng Zhang, Xiaoya Fan, Donglin Zhao, Zhengwei Cai, Jun Li, Dongdong Zheng, Xun He, Yongsong Luo, Yan Wang, Binwu Ying, Hong Yan, Shengjun Sun, Jing Zhang, Abdulmohsen Ali Alshehri, Feng Gong,* Yinyuan Zheng,* and Xuping Sun*

Synthesis of green ammonia (NH_3) via electrolysis of nitric oxide (NO) is extraordinarily sustainable, but multielectron/proton-involved hydrogenation steps as well as low concentrations of NO can lead to poor activities and selectivities of electrocatalysts. Herein, it is reported that oxygen-defective TiO_2 nanoarray supported on Ti plate ($\text{TiO}_{2-x}/\text{TP}$) behaves as an efficient catalyst for NO reduction to NH_3 . In 0.2 M phosphate-buffered electrolyte, such $\text{TiO}_{2-x}/\text{TP}$ shows competitive electrocatalytic NH_3 synthesis activity with a maximum NH_3 yield of $1233.2 \mu\text{g h}^{-1} \text{cm}^{-2}$ and Faradaic efficiency of 92.5%. Density functional theory calculations further thermodynamically faster NO deoxygenation and protonation processes on TiO_{2-x} (101) compared to perfect TiO_2 (101). And the low energy barrier of 0.7 eV on TiO_{2-x} (101) for the potential-determining step further highlights the greatly improved intrinsic activity. In addition, a Zn-NO battery is fabricated with $\text{TiO}_{2-x}/\text{TP}$ and Zn plate to obtain an NH_3 yield of $241.7 \mu\text{g h}^{-1} \text{cm}^{-2}$ while providing a peak power density of 0.84 mW cm^{-2} .

world population and it is also currently known as a clean, safe, and hydrogen-rich energy carrier to decarbonize the future energy storage and transportation process.^[1–4] The energy-intensive Haber-Bosch method adopted by NH_3 synthesis industries, nonetheless, remains as a fossil fuel-based technology with a significant carbon footprint.^[5] The development of energy-saving and carbon-neutral NH_3 synthetic routes is therefore of great interest. Electrosynthesis of NH_3 from nitrogen (N_2) and water (H^+ in acids), which can be powered by green energy, has aroused scientists' interest as an appealing and sustainable alternative.^[6–16] However, according to the thermodynamic principle, $\text{N}\equiv\text{N}$ bond requires robust dissociation energies (941 kJ mol^{-1}), which greatly limits the Faradaic efficiency (FE) and NH_3 yield. Moreover, the hydrogen

evolution catalysis makes high-rate N_2 -to- NH_3 hydrogenation unrealistic in the aqueous phase. Nitric oxide (NO) can be regarded as a suitable nitrogen source for generating NH_3 due to easier NO deoxygenation than the $\text{N}\equiv\text{N}$ bond breaking,

1. Introduction

Ammonia (NH_3) with extensive usage in the manufacture of fertilizers plays a critical role in supporting about half of the

Z. Li, J. Liang, L. Zhang, X. Fan, D. Zhao, J. Li, D. Zheng, X. He, Y. Luo, Y. Wang, B. Ying, H. Yan, X. Sun
Institute of Fundamental and Frontier Sciences
University of Electronic Science and Technology of China
Chengdu, Sichuan 610054, China
E-mail: xpsun@uestc.edu.cn

Q. Zhou, F. Gong
Key Laboratory of Energy Thermal Conversion and Control of Ministry of Education
School of Energy and Environment
Southeast University
Nanjing, Jiangsu 211189, China
E-mail: gongfeng@seu.edu.cn

Z. Cai, S. Sun
College of Chemistry
Chemical Engineering and Materials Science
Shandong Normal University
Jinan, Shandong 250014, China

J. Zhang
Interdisciplinary Materials Research Center
Institute for Advanced Study
Chengdu University
Chengdu 610106, China

A. A. Alshehri
Chemistry Department
Faculty of Science
King Abdulaziz University
P.O. Box 80203, Jeddah 21589, Saudi Arabia

Y. Zheng
Huzhou Key Laboratory of Translational Medicine
First People's Hospital affiliated to Huzhou University
Huzhou, Zhejiang 313000, China
E-mail: yinyuan_zheng@sina.com

The ORCID identification number(s) for the author(s) of this article can be found under <https://doi.org/10.1002/smll.202300291>.

DOI: 10.1002/smll.202300291

and the more positive reduction potential of NO to synthesize NH_3 than that of N_2 will make the electrochemical NO reduction reaction (NORR) more sustainable and efficient.^[17–22] Furthermore, it is believed that NO, a hazardous air contaminant widely present in exhaust gas from fossil fuel combustion, poses a major threat to both human health and ecological balance.^[23] Hence, it is reasonable to abate waste NO to NH_3 by electrocatalysis, which consumes less energy and eases the pressures on the environment. Despite the high reactivity of NO, the complex five-electron-coupled six-proton deep reduction to NH_3 and concurrent side-product/intermediate (N_2 , N_2O , NH_2OH , etc.) formation dramatically lowers NH_3 generation rates.^[24,25] The development of genuinely active and NH_3 -selective catalysts for NORR would enable the implementation of the technology in industries.

Much effort was devoted to ascertaining selectivities of noble metals, especially Pt, during the NO electrolysis, yet their NH_3 selectivities typically remained unsatisfactory because of the coproduction of other products (N_2O or NH_2OH).^[26–28] Recent NORR catalysts including MoS_2 nanoarray,^[21] a- $\text{B}_{2.6}\text{C}/\text{TiO}_2$,^[29] single-atom Nb sites supported on B,N co-doped carbon nanotubes (Nb-SA/BNC),^[30] Cu foam,^[31] etc. can selectively produce NH_3 from NO, but metal complexes to increase the solubility of NO or high-purity of NO are needed for enhanced performance. Encouragingly, TiO_2 , one of the cheapest, most eco-friendly, and highly durable materials, is seen as a promising electrode material for electrocatalysis.^[32–38] Notably, limited active sites and low electrical conductivity of TiO_2 usually lead to poor catalytic performance. The design of TiO_2 with 1) abundant available active sites that prefer to generate NH_3 via deep NO reduction rather than following N–N coupling pathways to N_2 or N_2O , 2) morphology conducive to electron pass/mass transport, and 3) improved electrical conductivity for NO electrolysis would provide us high-performance catalysts and meaningful advances in identifying economical and high-active NH_3 -producing NORR catalysts, whereas related works have been rarely reported.

Herein, we report high-efficiency NH_3 electrosynthesis on oxygen vacancies (OVs) defect-engineered TiO_{2-x} using low-concentration NO as the reactant. An open nanoarray architecture of TiO_{2-x} further maximizes the utilization of optimized catalytic sites for NO adsorption and subsequent activation. Accordingly, such TiO_{2-x} nanoarray on Ti plate ($\text{TiO}_{2-x}/\text{TP}$) acts as a superb NH_3 -producing 3D nanocatalyst for NO electrolysis in neutral media, attaining a great yield of $1233.2 \mu\text{g h}^{-1} \text{cm}^{-2}$ and high FE of 92.5%, superior to many state-of-the-art NORR catalysts (Table S1, Supporting Information). Density functional theory (DFT) calculations identify $^*\text{NH}_2$ protonation to $^*\text{NH}_3$ on TiO_{2-x} (101) as the potential-determining step with an uphill energy barrier of only 0.7 eV. Importantly, unlike the difficult formation of $^*\text{NO}$ on perfect TiO_2 (101), NO adsorption on the TiO_{2-x} (101) results in a dramatic energy drop of ≈ 2.1 eV, reflecting more favorable adsorption properties of defective TiO_{2-x} . Additionally, our $\text{TiO}_{2-x}/\text{TP}$ is directly applied in a homemade Zn–NO battery as a robust and kinetically fast cathode to afford a peak power density of 0.84 mW cm^{-1} and an NH_3 yield as high as $241.7 \mu\text{g h}^{-1} \text{cm}^{-2}$.

2. Results and Discussion

2.1. Morphology and Structure Characterizations

The synthetic process of $\text{TiO}_{2-x}/\text{TP}$ is shown in Figure 1a including hydrothermal treatment, H^+ exchange, and H_2/Ar annealing. X-ray diffraction (XRD) patterns for $\text{TiO}_{2-x}/\text{TP}$ and TiO_2 show typical peaks at 25.4° , 37.9° , 48.1° , 54.0° , and 55.2° , which correspond to the (101), (004), (200), (105), and (211) facets of TiO_2 (JCPDS (Joint Committee on Powder Diffraction Standards) No. 73-1764) (Figure 1b).^[39] The diffraction peaks at 40.2° and 53.0° attributed to (101) and (102) facets of Ti (JCPDS No. 44-1294). But, in detail, the sharp diffraction peak of (101) for $\text{TiO}_{2-x}/\text{TP}$ becomes weak compared with TiO_2/TP . Scanning electron microscopy (SEM) image in Figure 1c reveals the smooth nanoribbons of $\text{TiO}_{2-x}/\text{TP}$, which shows no obvious difference with TiO_2/TP (Figure S1, Supporting Information). Energy-dispersive X-ray (EDX) mapping images demonstrate that elements of Ti and O are uniformly distributed on the surface of $\text{TiO}_{2-x}/\text{TP}$ (Figure 1d). Transmission electron microscopy (TEM) image also reveals the TiO_{2-x} with uniform and no obvious defects of morphology, which are consistent with SEM results (Figure 1e). The lattice fringe with interplanar distances of 0.351 nm is observed from high-resolution TEM (HRTEM) shown in Figure 1f, which can be ascribed to the (101) facet of the TiO_2 phase. Notably, the lattice fringe defects can be detected, which suggests the successful formation of a defect-rich structure.

In order to further verify the existence of OVs, electron paramagnetic resonance (EPR) test is performed. A pair of sharp peaks of $\text{TiO}_{2-x}/\text{TP}$ exhibit at $g = 2.002$ (Figure 1g), indicating electron trapping at oxygen defects, which is in contrast to no obvious peaks of TiO_2/TP .^[40] To investigate the surface chemical bonding of $\text{TiO}_{2-x}/\text{TP}$, X-ray photoelectron spectroscopy (XPS) analysis is implemented. As shown in Ti 2p spectrum, the distinct peaks of Ti $2p_{3/2}$ and Ti $2p_{1/2}$ appear at 457.9 and 463.8 eV belonging to Ti^{4+} of the TiO_2/TP (Figure 1h).^[41,42] Nevertheless, the peaks Ti $2p_{3/2}$ and Ti $2p_{1/2}$ of $\text{TiO}_{2-x}/\text{TP}$ shift to the lower binding energy compared with TiO_2/TP , which attribute to decreased Ti oxidation state.^[43] As for O 1s (Figure 1i), peaks at 529.4, 531.2, and 532.6 eV are related to lattice O, OVs, and physisorbed H_2O , for TiO_2/TP , respectively.^[44–46] Furthermore, the area of OVs relative to the sum area of all peaks [$S_{(\text{OVs})}/(S_{(\text{physisorbed H}_2\text{O})} + S_{(\text{OVs})} + S_{(\text{lattice O})})$] is 16.7% for $\text{TiO}_{2-x}/\text{TP}$, indicating that more OVs in $\text{TiO}_{2-x}/\text{TP}$ are constructed than TiO_2/TP (13.8%). Above observations suggest the successful construction of OVs in $\text{TiO}_{2-x}/\text{TP}$.

2.2. Electrochemical Performance Measurements

A three-electrode setup of an H-shape electrolytic reactor containing 0.2 M phosphate-buffered solution (PBS) with flowing NO gas is used to test the electrochemical NORR performance of $\text{TiO}_{2-x}/\text{TP}$. The system of three electrodes contains a work electrode (self-supporting $\text{TiO}_{2-x}/\text{TP}$), a reference electrode (Ag/AgCl), and a counter electrode (graphite electrode). During the test, the gas of NO (10 vol%) with a flowing speed

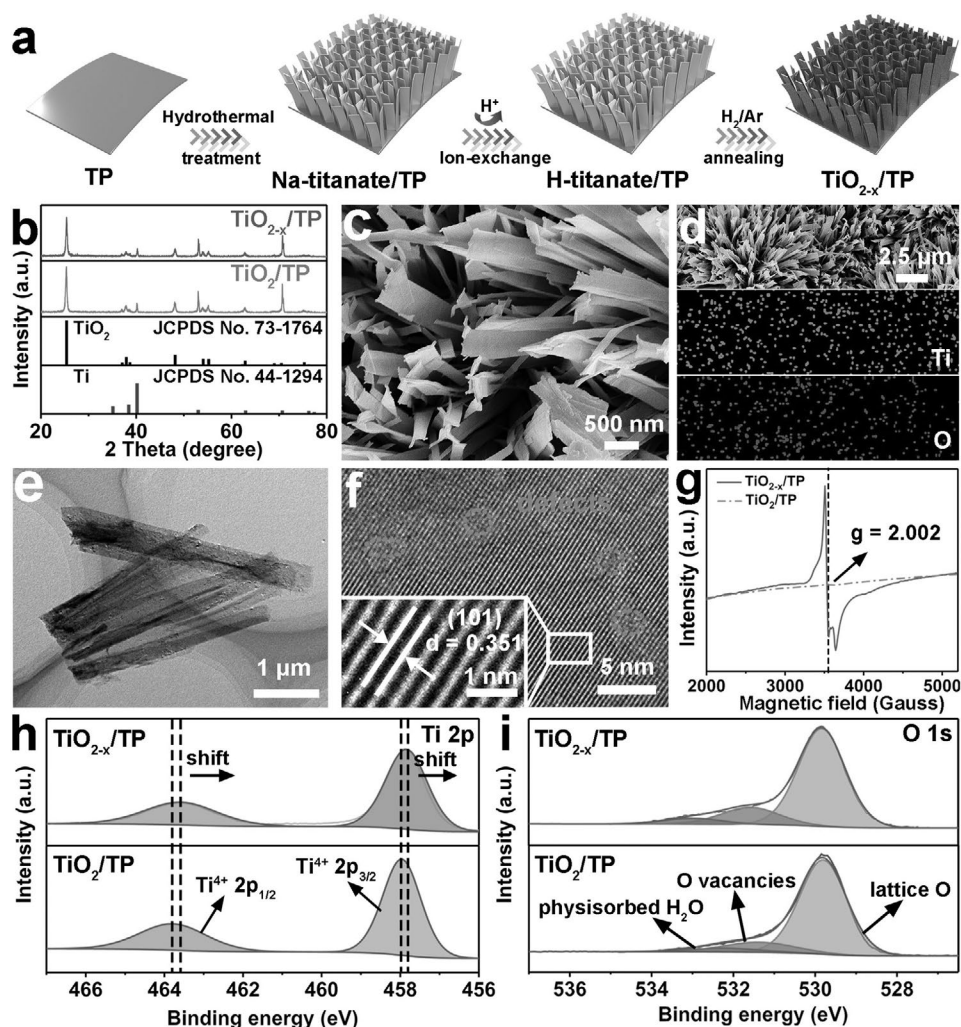


Figure 1. a) Schematic description of $\text{TiO}_{2-x}/\text{TP}$ synthesis. b) XRD patterns of $\text{TiO}_{2-x}/\text{TP}$ and TiO_2/TP . c) SEM image of $\text{TiO}_{2-x}/\text{TP}$. d) SEM and EDX elemental mapping images of $\text{TiO}_{2-x}/\text{TP}$. e,f) TEM and HRTEM images of the TiO_{2-x} . g) EPR spectra of TiO_{2-x} and TiO_2 . XPS spectra of $\text{TiO}_{2-x}/\text{TP}$ and TiO_2/TP in h) Ti 2p and i) O 1s regions.

of 50 sccm is used as inlet gas. Potentials are reported on the reversible hydrogen electrode scale. From **Figure 2a**, the linear sweep voltammetry (LSV) curves of TiO_2/TP and $\text{TiO}_{2-x}/\text{TP}$ electrodes are obtained with a potential range of 0.0 to -1.0 V. In NO-saturated 0.2 M PBS, an obvious current density gap arose between -0.3 and -0.8 V, which indicates the effective NORR occurs over $\text{TiO}_{2-x}/\text{TP}$ at this potential range. The LSV curve for $\text{TiO}_{2-x}/\text{TP}$ electrode is observed with a larger current density than TiO_2/TP , which proves the formation of OV can improve the electrical conductivity of $\text{TiO}_{2-x}/\text{TP}$. Furthermore, the almost same LSV curves of bare TP in Ar- and NO-saturated 0.2 M PBS prove the TP with no NORR activity. To further investigate the NORR activity of $\text{TiO}_{2-x}/\text{TP}$, NH_3 yields and FEs are obtained from chronoamperometry (CA) measurements under the potential between -0.3 and -0.8 V. The CA curves and related UV-vis curves of NH_3 at various potentials are given in **Figure S2** in the Supporting Information. The NH_3 yields and FEs of $\text{TiO}_{2-x}/\text{TP}$ can be calculated based on the NH_3 calibration curve (**Figure S3**, Supporting Information) and **Figure 2b**

shows their maximum NH_3 yields achieving $1233.2 \mu\text{g h}^{-1} \text{cm}^{-2}$ at -0.7 V and FEs up to 92.5% at -0.4 V, which indicates that $\text{TiO}_{2-x}/\text{TP}$ is an efficient catalyst and its performance is higher than many other reported NORR electrocatalysts (Table S1, Supporting Information). In order to investigate the side reaction in the process of NORR, we use gas chromatography (GC) to detect the by-products of N_2 and H_2 . As shown in **Figure 2b**, N_2 is detected at low potential and decreases as potential increasing. However, with the increase of current density, the hydrogen evolution reaction (HER) is enhanced according to the result of GC analysis (**Figure 2b**). Furthermore, as depicted in **Figure 2c**, $\text{TiO}_{2-x}/\text{TP}$ could yield NH_3 of $460.1 \mu\text{g h}^{-1} \text{cm}^{-2}$ while achieving supreme FE of 92.5% at -0.4 V, much higher than TiO_2/TP ($337.5 \mu\text{g h}^{-1} \text{cm}^{-2}$ and 48.7% at the same potential). To confirm that NH_3 is produced by the electrocatalytic NO reduction to NH_3 on $\text{TiO}_{2-x}/\text{TP}$, the electrochemical NORR tests at -0.4 V in Ar-saturated 0.2 M PBS and yield NH_3 only about $8.2 \mu\text{g h}^{-1} \text{cm}^{-2}$. Long-time electrolysis at open-circuit potential is also detected with a minute NH_3 yield. The fresh electrolyte is

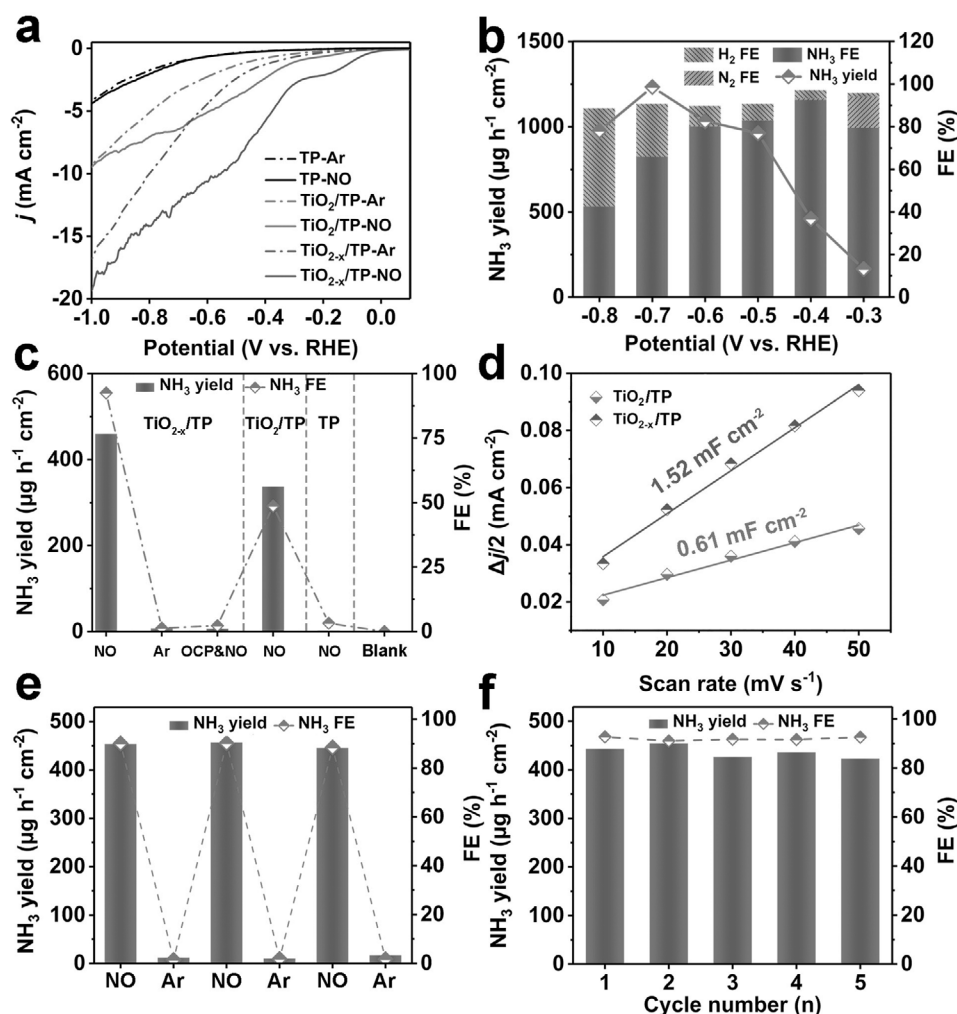


Figure 2. a) LSV curves of TP, TiO_2/TP , and $\text{TiO}_{2-x}/\text{TP}$ in Ar- and NO-saturated 0.2 M PBS. b) FEs of the major reductive products and NH_3 yields for $\text{TiO}_{2-x}/\text{TP}$ at different potentials. c) Comparison of NH_3 yields and FEs of different catalysts at -0.4 V under different conditions. d) Capacitive current densities of TiO_2/TP and $\text{TiO}_{2-x}/\text{TP}$ at 0.61 V as a function of the scan rate. e) NH_3 yields and FEs of $\text{TiO}_{2-x}/\text{TP}$ during alternating cycles test in Ar- and NO-saturated 0.2 M PBS. f) NH_3 yields and FEs of $\text{TiO}_{2-x}/\text{TP}$ under cycling tests at -0.4 V in NO-saturated 0.2 M PBS.

tested to eliminate the background contribution. These results indicate that a trace amount of NH_3 is produced by the above tests, which eliminates the possible influence of the device and electrolyte. Similarly, bare TP is also tested at -0.4 V and shows negligible NH_3 yield and FE, ruling out its influence on NORR. Figure S4 in the Supporting Information shows the UV-vis spectrum corresponding to the above tests. The effect of pH on NORR of $\text{TiO}_{2-x}/\text{TP}$ is also conducted. From Figure S5 in the Supporting Information, the highest FE of 92.5% is obtained under a neutral medium. As shown in Figure 2d, the electrochemical active surface area of TiO_2/TP and $\text{TiO}_{2-x}/\text{TP}$ can be calculated by the double-layer capacitance (C_{dl}) based on non-Faraday region cyclic voltammetry curves of them (Figure S6, Supporting Information).^[47] The calculated C_{dl} of $\text{TiO}_{2-x}/\text{TP}$ (1.52 mF cm^{-2}) is superior to TiO_2/TP (0.61 mF cm^{-2}), which further confirms that OV contribute to the exposure of active sites. Alternating electrolysis on $\text{TiO}_{2-x}/\text{TP}$ is performed at -0.4 V (Figure 2e), a few amounts of NH_3 can be detected in Ar-saturated electrolyte, and their UV-vis spectra are shown in

Figure S7 in the Supporting Information. The cycling test is carried out to prove the good stability of $\text{TiO}_{2-x}/\text{TP}$ for catalyzing NO reduction to NH_3 . From Figure 2f, the result indicates that the NH_3 yields and FEs for $\text{TiO}_{2-x}/\text{TP}$ have slight changes for five reaction cycles, and the corresponding UV-vis absorbance curves are shown in Figure S8 in the Supporting Information. The long-term operations of TiO_2/TP and $\text{TiO}_{2-x}/\text{TP}$ at -0.4 V are tested for 12 h (Figure S9, Supporting Information). The steady current density throughout the 12 h period suggests high stability of $\text{TiO}_{2-x}/\text{TP}$ and still maintains its initial morphology after the stability test (Figure S10, Supporting Information). All of the above catalytic performance tests confirm that $\text{TiO}_{2-x}/\text{TP}$ is an effective and durable catalyst for NORR.

2.3. DFT calculations

To get insight into the mechanism of NORR on TiO_{2-x} , DFT calculation is performed to investigate the elementary step

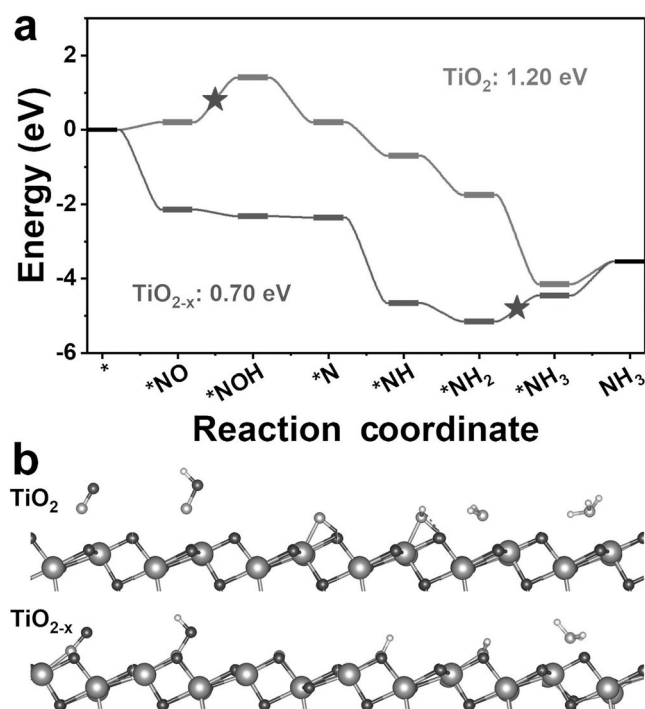


Figure 3. a) Gibbs free energy profiles of NORR on the TiO_2 (101) and TiO_{2-x} (101) facets. b) Corresponding atomic configurations. Blue, red, white, and pink spheres denote the Ti, O, N, and H atoms, respectively.

of the whole NORR reaction process. Herein, we chose the five-coordinated Ti on the exposed (101) facet of TiO_{2-x} as an active site for NORR according to the HRTEM figure while an oxygen atom on the surface is removed to simulate the oxygen vacancy. **Figure 3a** exhibits the reaction-free energy profiles for different intermediates of NORR on TiO_2 and TiO_{2-x} surface. The calculational results indicate that the adsorption of NO is dramatically enhanced on TiO_{2-x} with lower adsorption energy and shorter distance between NO and Ti active site (**Figure 3b**), which can facilitate the following activation of NO. Thus, the maximum energy barrier of all elementary steps of NORR on TiO_{2-x} (0.7 eV) is much lower than that on pristine TiO_2 (1.2 eV), demonstrating that the catalytic performance of TiO_{2-x} is efficiently improved. What is more, the adsorption energy of $\ast\text{H}$ on the OV of TiO_2 (−0.44 eV) is much larger than that of $\ast\text{NO}$ on TiO_{2-x} (−2.14 eV), indicating that the TiO_{2-x} can efficiently suppress the competing HER (**Figure S11a**, Supporting Information). Ab initio molecular dynamics (AIMD) simulation is performed under 300 K for 10 ps to evaluate the stability of the synthesized catalyst. It can be observed that the free energy of the TiO_{2-x} vibrated around the equilibrium state and no obvious distortion happened after the AIMD simulation, confirming that the oxygen vacancy active site on the TiO_{2-x} surface is stable (**Figure S11b**, Supporting Information).

2.4. Measurements of Battery

Zn-NO batteries, as the potential practical application, can simultaneously achieve NO elimination, NH_3 synthesis, and

energy release. As we expected, a Zn-NO battery is fabricated with the $\text{TiO}_{2-x}/\text{TP}$ cathode, the Zn plate anode, and a bipolar membrane between catholyte (0.2 M NO-saturated PBS) and anolyte (1.0 M KOH). For the Zn-NO battery, its discharge process contains NORR occurring on $\text{TiO}_{2-x}/\text{TP}$, and the oxidizing reaction on the Zn anode (**Figure 4a**). As shown in **Figure 4b**, the as-prepared battery delivers a maximum power density (0.84 mW cm^{-2}) superior to that of the compared device (0.29 mW cm^{-2}). The result confirms that the excellent performance of $\text{TiO}_{2-x}/\text{TP}$ as a cathodic material contributes to achieving high power densities, meanwhile enlarging the output currents of Zn-NO battery. The voltage of the battery nearly not changed under discharging test at various current densities (1, 2, 3, and 4 mA cm^{-2}) (**Figure 4c**). What is more, the battery shows considerable NH_3 productivity at various currents (**Figure 4d**) and the corresponding UV-vis absorption curves are shown in **Figure S12** in the Supporting Information. As-prepared Zn-NO battery also provides a stable open circuit voltage of 1.56 V versus Zn (**Figure S13**, Supporting Information). In **Figure 4e**, the Zn-NO battery could produce a maximum NH_3 yield of $241.7 \mu\text{g h}^{-1} \text{ cm}^{-2}$, significantly outperforming the most recent metal- N_2 battery devices.^[48–50] Thus, a novel gas-based energy conversion device involving NO electrochemistry reduction is fabricated for wide use.

3. Conclusions

In summary, our 3D $\text{TiO}_{2-x}/\text{TP}$ is an efficient and stable NORR electrocatalyst, achieving selective NH_3 generation at a high yield and FE ($1233.2 \mu\text{g h}^{-1} \text{ cm}^{-2}$ at −0.7 V and 92.5% at −0.4 V) in neutral media. DFT calculations reveal the mechanisms of overall NO-to- NH_3 reduction process and the positive influence of OV defects in improving the adsorption/conversion of intermediates on defective TiO_{2-x} . The aqueous Zn-NO battery fabricated with $\text{TiO}_{2-x}/\text{TP}$ and Zn can achieve maximum NH_3 yield and power density of $241.7 \mu\text{g h}^{-1} \text{ cm}^{-2}$ and 0.84 mW cm^{-2} . This work not only provides us with an attractive catalyst material for NO electroreduction at low concentrations of NO but would up a new avenue to the rational design and development of Ti-based nanocatalysts for application toward NO electrolysis.

Supporting Information

Supporting Information is available from the Wiley Online Library or from the author.

Acknowledgements

This work was supported by the National Natural Science Foundation of China (No. 22072015).

Conflict of Interest

The authors declare no conflict of interest.

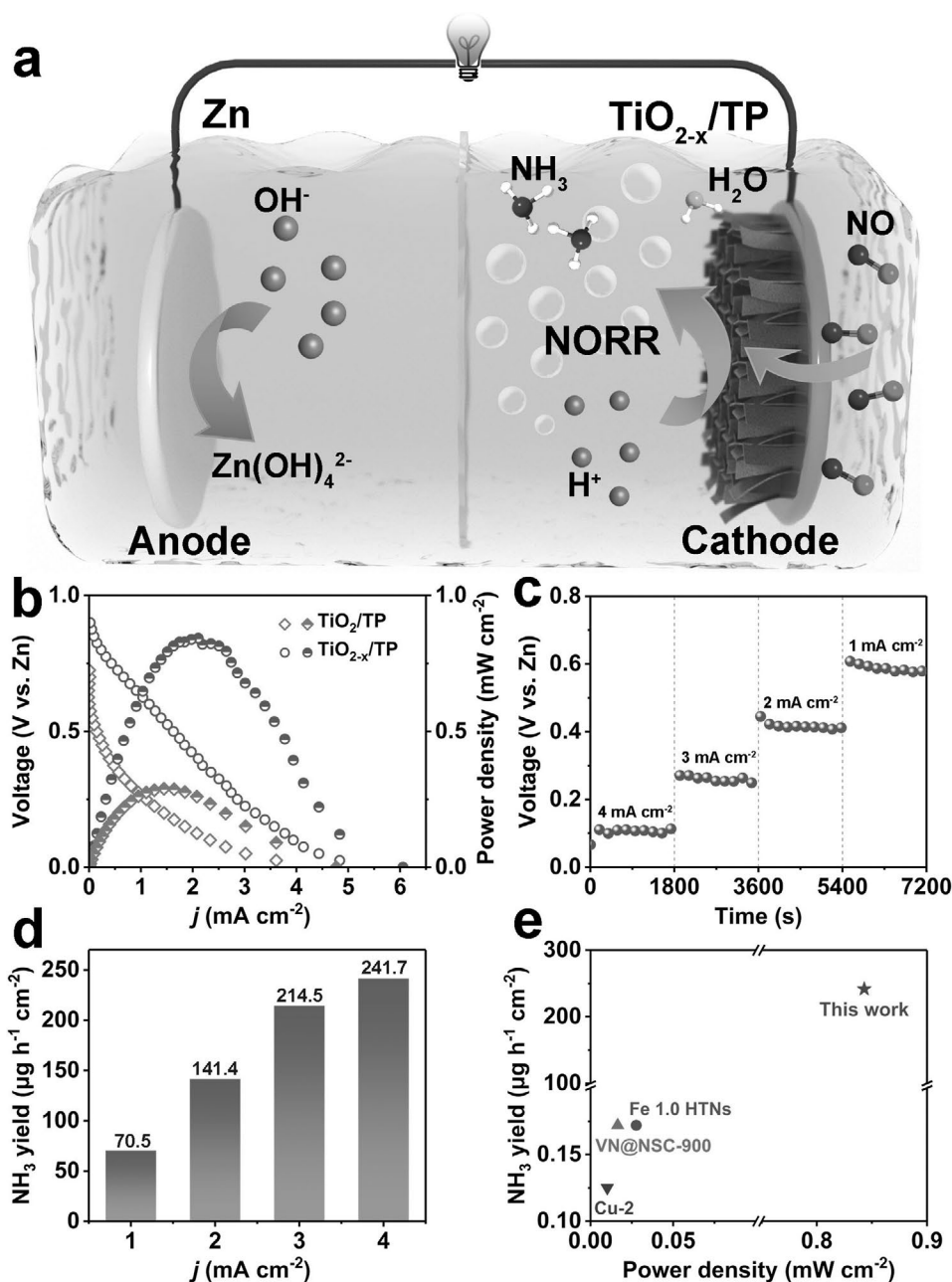


Figure 4. a) Schematic description of the Zn-NO battery. b) Polarization and power density plots of TiO_2/TP and $\text{TiO}_{2-x}/\text{TP}$ -based Zn-NO battery. c) Discharging tests at various current densities. d) NH_3 yields at different current densities. e) Comparison of NH_3 yield and power density of $\text{TiO}_{2-x}/\text{TP}$ -based Zn-NO battery with reported metal- N_2 batteries.

Data Availability Statement

The data that support the findings of this study are available from the corresponding author upon reasonable request.

Keywords

ambient ammonia synthesis, nitric oxide (NO) reduction reaction, oxygen vacancies, theoretical calculations, TiO_{2-x} nanoarray

Received: January 10, 2023

Revised: February 17, 2023

Published online: March 15, 2023

- [1] J. Liang, Q. Liu, A. A. Alshehri, X. Sun, *Nano Res. Energy* **2022**, 1, e9120010.
- [2] R. Schlögl, *Angew. Chem., Int. Ed.* **2003**, 42, 2004.
- [3] V. Smil, *Nature* **1999**, 400, 415.
- [4] H. Huang, F. Li, Q. Xue, Y. Zhang, S. Yin, Y. Chen, *Small* **2019**, 15, 1903500.
- [5] G. Ertl, *Catalytic Ammonia Synthesis* (Ed: J. R. Jennings), Plenum, New York **1991**.
- [6] Y. Luo, Q. Li, Y. Liu, K. Chu, *J. Mater. Chem. A* **2022**, 10, 1742.
- [7] Y. Ren, C. Yu, X. Tan, H. Huang, Q. Wei, J. Qiu, *Energy Environ. Sci.* **2021**, 14, 1176.
- [8] D. Chanda, R. Xing, T. Xu, Q. Liu, Y. Luo, S. Liu, R. A. Tufa, T. H. Dolla, T. Montini, X. Sun, *Chem. Commun.* **2021**, 57, 7335.

- [9] Q. Li, P. Shen, Y. Tian, X. Li, K. Chu, *J. Colloid Interface Sci.* **2022**, 606, 204.
- [10] S. Gao, Y. Zhu, Y. Chen, M. Tian, Y. Yang, T. Jiang, Z. Wang, *Mater. Today* **2019**, 28, 17.
- [11] Y. Sun, W. Wu, L. Yu, S. Xu, Y. Zhang, L. Yu, B. Xia, S. Ding, M. Li, L. Jiang, J. Duan, J. Zhu, S. Chen, *Carbon Energy* **2022**, <https://doi.org/10.1002/cey2.263>.
- [12] D. Yao, C. Tang, L. Li, B. Xia, A. Vasileff, H. Jin, Y. Zhang, S. Qiao, *Adv. Energy Mater.* **2020**, 10, 2001289.
- [13] X. Cui, C. Tang, Q. Zhang, *Adv. Energy Mater.* **2018**, 8, 1800369.
- [14] C. Liu, S. Li, Z. Li, L. Zhang, H. Chen, D. Zhao, S. Sun, Y. Luo, *Sustainable Energy Fuels* **2022**, 6, 3344.
- [15] P. Wei, Q. Geng, A. I. Channa, X. Tong, Y. Luo, S. Lu, G. Chen, S. Gao, Z. Wang, X. Sun, *Nano Res.* **2020**, 13, 2967.
- [16] Y. Yao, S. Zhu, H. Wang, H. Li, M. Shao, *J. Am. Chem. Soc.* **2018**, 140, 1496.
- [17] Y. Lin, J. Liang, H. Li, L. Zhang, T. Mou, T. Li, L. Yue, Y. Ji, Q. Liu, Y. Luo, N. Li, B. Tang, Q. Wu, M. S. Hamdy, D. Ma, X. Sun, *Mater. Today Phys* **2022**, 22, 100611.
- [18] D. Qi, F. Lv, T. Wei, M. Jin, G. Meng, S. Zhang, Q. Liu, W. Liu, D. Ma, M. S. Hamdy, J. Luo, X. Liu, *Nano Res. Energy* **2022**, 1, e9120022.
- [19] Q. Liu, Y. Lin, L. Yue, J. Liang, L. Zhang, T. Li, Y. Luo, M. Li, J. You, A. A. Alshehri, Q. Kong, X. Sun, *Nano Res.* **2022**, 15, 5032.
- [20] H. Li, J. Long, H. Jing, J. Xiao, *Nat. Commun.* **2023**, 14, 112.
- [21] L. Zhang, J. Liang, Y. Wang, T. Mou, Y. Lin, L. Yue, T. Li, Q. Liu, Y. Luo, N. Li, B. Tang, Y. Liu, S. Gao, A. A. Alshehri, X. Guo, D. Ma, X. Sun, *Angew. Chem., Int. Ed.* **2021**, 60, 25263.
- [22] T. Mou, J. Liang, Z. Ma, L. Zhang, Y. Lin, T. Li, Q. Liu, Y. Luo, Y. Liu, S. Gao, H. Zhao, A. M. Asiri, D. Ma, X. Sun, *J. Mater. Chem. A* **2021**, 9, 24268.
- [23] H. Huo, Q. Zhang, F. Liu, K. He, *Environ. Sci. Technol.* **2013**, 47, 1711.
- [24] L. L. J. Janssen, M. M. J. Pieterse, E. Barendrecht, *Electrochim. Acta* **1977**, 22, 27.
- [25] I. Paseka, J. Voňková, *Electrochim. Acta* **1980**, 25, 1251.
- [26] H. J. Chun, V. Apaja, A. Clayborne, K. Honkala, J. Greeley, *ACS Catal.* **2017**, 7, 3869.
- [27] J. Choi, H. L. Du, C. K. Nguyen, B. H. R. Suryanto, A. N. Simonov, D. R. MacFarlane, *ACS Energy Lett.* **2020**, 5, 2095.
- [28] M. Shibata, K. Murase, N. Furuya, *J. Appl. Electrochem.* **1998**, 28, 1121.
- [29] J. Liang, P. Liu, Q. Li, T. Li, L. Yue, Y. Luo, Q. Liu, N. Li, B. Tang, A. A. Alshehri, I. Shakir, P. O. Agboola, C. Sun, X. Sun, *Angew. Chem., Int. Ed.* **2022**, 61, e202202087.
- [30] X. Peng, Y. Mi, H. Bao, Y. Liu, D. Qi, Y. Qiu, L. Zhuo, S. Zhao, J. Sun, X. Tang, J. Luo, X. Liu, *Nano Energy* **2020**, 78, 105321.
- [31] J. Long, S. Chen, Y. Zhang, C. Guo, X. Fu, D. Deng, J. Xiao, *Angew. Chem., Int. Ed.* **2020**, 59, 9711.
- [32] Y. Guo, R. Zhang, S. Zhang, Y. Zhao, Q. Yang, Z. Huang, B. Dong, C. Zhi, *Energy Environ. Sci.* **2021**, 14, 3938.
- [33] S. Li, J. Liang, P. Wei, Q. Liu, L. Xie, Y. Luo, X. Sun, *eScience* **2022**, 2, 382.
- [34] J. Chen, W. Zhang, H. Li, W. Li, D. Zhao, *SusMat* **2021**, 1, 174.
- [35] R. Jia, Y. Wang, C. Wang, Y. Ling, Y. Yu, B. Zhang, *ACS Catal.* **2020**, 10, 3533.
- [36] L. Ouyang, X. He, Y. Sun, L. Zhang, D. Zhao, S. Sun, Y. Luo, D. Zheng, A. M. Asiri, Q. Liu, J. Zhao, X. Sun, *Inorg. Chem. Front.* **2022**, 9, 6602.
- [37] W. P. Utomo, H. Wu, Y. H. Ng, *Small* **2022**, 18, 2200996.
- [38] Q. Li, C. Fang, Z. Yang, B. Yu, *Small* **2022**, 18, 2201343.
- [39] M. Yao, H. Wang, R. Qian, T. Yao, J. Shi, Y. Cheng, *Inorg. Chem. Front.* **2021**, 8, 5024.
- [40] K. Qian, L. Du, X. Zhu, S. Liang, S. Chen, H. Kobayashi, X. Yan, M. Xu, Y. Dai, R. Li, *J. Mater. Chem. A* **2019**, 7, 14592.
- [41] F. Li, B. Dong, S. Feng, *Int. J. Hydrogen Energy* **2019**, 44, 29986.
- [42] Y. Zhao, C. Li, X. Liu, F. Gu, H. L. Du, L. Shi, *Appl. Catal., B* **2008**, 79, 208.
- [43] J. Yang, Y. Guo, R. Jiang, F. Qin, H. Zhang, W. Lu, J. Wang, J. Yu, *J. Am. Chem. Soc.* **2018**, 140, 8497.
- [44] Z. Geng, X. Kong, W. Chen, H. Su, Y. Liu, F. Cai, G. Wang, J. Zeng, *Angew. Chem., Int. Ed.* **2018**, 57, 6054.
- [45] L. Li, J. Yan, T. Wang, Z. Zhao, J. Zhang, J. Gong, N. Guan, *Nat. Commun.* **2015**, 6, 5881.
- [46] H. Gao, G. Hu, J. Sui, C. Mu, W. Shangguan, M. Kong, W. Shentu, *Appl. Catal., B* **2018**, 226, 337.
- [47] J. Kibsgaard, Z. Chen, B. N. Reinecke, T. F. Jaramillo, *Nat. Mater.* **2012**, 11, 963.
- [48] X. Lv, X. Liu, L. Gao, Y. Liu, Z. Yuan, *J. Mater. Chem. A* **2021**, 9, 4026.
- [49] X. Lv, Y. Liu, Y. Wang, X. Liu, Z. Yuan, *Appl. Catal., B* **2021**, 280, 119434.
- [50] C. Du, Y. Gao, J. Wang, W. Chen, *Chem. Commun.* **2019**, 55, 12801.